

# Graphene as a Tunable Nonradiative Bath for Moiré Excitons

Katsunori Wakabayashi<sup>1,\*</sup>

<sup>1</sup>*Research Center for Materials Nanoarchitectonics (MANA),  
National Institute for Materials Science (NIMS), Namiki 1-1, Tsukuba 305-0044, Japan*  
(Dated: June 30, 2026)

A minimal theory for the nonradiative transfer of energy from a two-dimensional (2D) exciton—especially a moiré-localized exciton—to a nearby graphene layer is presented. Starting from Fermi’s golden rule, the transfer rate is written as the overlap between the exciton near-field spectrum and the long-wavelength electronic loss function of graphene, weighted by an exciton form factor. In the point-dipole limit the framework reproduces the established  $\Gamma_{\text{ET}} \propto z^{-4}$  law for energy transfer to graphene. Including the finite spatial extent of a moiré exciton through a Gaussian form factor with localization length  $\ell_X$ , we show that high-momentum components of the near field are filtered out for  $z \lesssim \ell_X$ , so that the transfer rate—and hence the photoluminescence (PL) quenching—can serve as a probe of exciton localization. Treating graphene as a gate-tunable bath, a Pauli-blocking model predicts that interband electron–hole excitations are strongly suppressed once  $2|\mu_F|$  approaches  $\hbar\omega$ , partially restoring PL intensity and lifetime. Benchmarking against the full random-phase-approximation loss function of doped graphene confirms the minimal model to within a few percent over the relevant distance range for representative near-infrared exciton parameters. We map the resulting PL observables over experimentally relevant ranges of spacer thickness, localization length, emission energy, and Fermi level, and identify when graphene-induced quenching dominates the optical response of transition-metal dichalcogenide/hexagonal boron nitride/graphene heterostructures. A graphene gate thus acts not as a passive electrostatic element but as a tunable 2D electronic reservoir whose long-wavelength response can be probed through exciton PL quenching.

## I. INTRODUCTION

When an excited emitter is placed near a conducting or semimetallic system, it can relax by transferring its energy nonradiatively to electronic excitations of that system instead of emitting a photon. For graphene, Swathi and Sebastian showed using a tight-binding model and the Dirac-cone approximation that the resonance energy-transfer (ET) rate from a point dye molecule scales as  $z^{-4}$  with the emitter–graphene distance  $z$  [1, 2], much longer ranged than the  $R^{-6}$  Förster law of molecular fluorescence resonance energy transfer [3]. This distance scaling has been observed experimentally for individual quantum emitters and semiconductor nanostructures [4–6], and the relaxation pathway has been shown to be electrically controllable through the graphene Fermi level [7, 8]. On the theory side, the graphene fluorescence-quenching problem has been revisited with the full electronic response of graphene, clarifying the role of its loss function and of longitudinal and transverse plasmons [9, 10].

Two-dimensional (2D) semiconductors and their moiré superlattices provide a new and qualitatively richer setting for this physics. The optical response of monolayer and bilayer transition-metal dichalcogenides (TMDCs) is dominated by tightly bound excitons with binding energies of hundreds of meV [11, 12]. In TMDC heterobilayers, interlayer excitons can be trapped in the moiré potential, forming arrays of localized emitters whose spatial extent  $\ell_X$  ranges from a few to tens of nanometers [13–18]; the theory and broader phenomenology of these

moiré-trapped emitters are reviewed in Refs. [19–21], and they act as gate-tunable quantum-light sources [22]. These devices commonly include nearby graphene or graphite layers acting as gates or contacts, separated from the excitons by only a few nanometers of hexagonal boron nitride (hBN). The same graphene or graphite electrode used for electrostatic control therefore sits within the range over which it can extract excitation energy from the excitons.

The nonradiative mechanism itself is general: it is not specific to moiré excitons but operates for any emitter—a dye molecule, a quantum dot, a free or disorder-localized monolayer exciton—placed near a 2D electronic bath. What distinguishes these cases is the emitter’s spatial extent, which enters the transfer rate through a form factor  $F_X(q)$  (Table I). A point dipole has  $F_X \rightarrow 1$  and recovers the Swathi–Sebastian result; a delocalized monolayer exciton has an effective  $F_X$  set by coherence, temperature, and disorder, none of them easily controlled. A moiré exciton is the cleanest realization: its center-of-mass wave function is localized by the moiré potential, so its localization length  $\ell_X$  is an *intrinsic and tunable* parameter—set by twist angle, moiré-potential depth, and registry. This makes proximity quenching a quantitative, controllable probe of exciton localization, and is why we take moiré excitons as the primary application of an otherwise general formalism.

In this work we reformulate graphene-induced fluorescence quenching for the modern context of moiré excitons. Related resonance-energy-transfer problems involving graphene and localized emitters—quantum dots, defect-bound single-photon emitters, and moiré-trapped excitons—have been studied within the random-phase

\* WAKABAYASHI.Katsunori@nims.go.jp

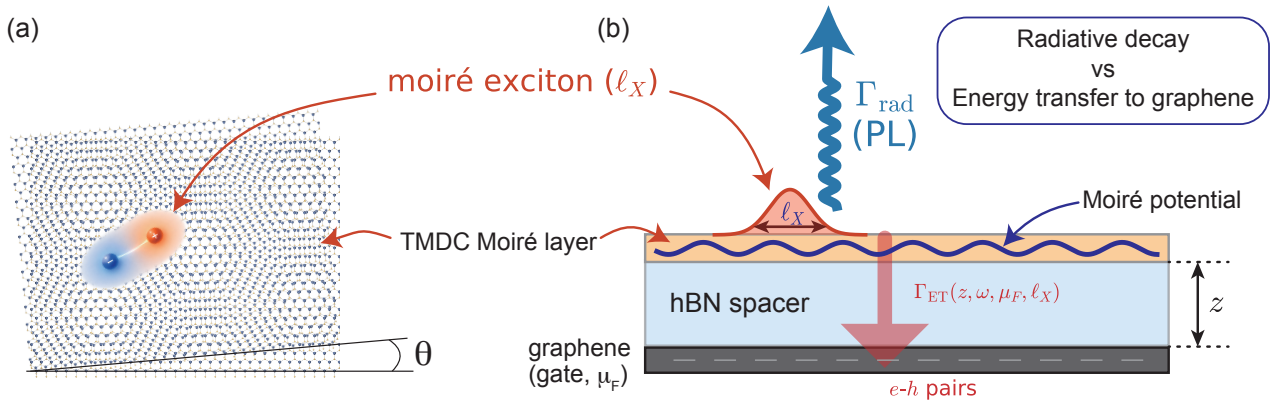


FIG. 1. (a) A moiré exciton—a bound electron–hole pair of localization length  $\ell_X$ —trapped in the moiré superlattice formed at twist angle  $\theta$ . (b) Device cross section: the exciton in the transition-metal dichalcogenide moiré layer can decay radiatively ( $\Gamma_{\text{rad}}$ , PL) or transfer its energy nonradiatively across a hexagonal boron nitride spacer of thickness  $z$  to electron–hole pairs in a graphene gate at Fermi level  $\mu_F$  [ $\Gamma_{\text{ET}}(z, \omega, \mu_F, \ell_X)$ ], the channel studied here.

TABLE I. Emitters near a 2D electronic bath, classified by the (amplitude) exciton form factor  $F_X(q)$ ; the rate (5) carries  $|F_X(q)|^2$ .

emitter	$F_X(q)$	localization
point dipole / molecule	1	none ( $z^{-4}$ limit)
free exciton	effective	weak, uncontrolled
disorder-localized	$e^{-q^2 \ell_{\text{dis}}^2/4}$	random
moiré exciton	$e^{-q^2 \ell_X^2/4}$	<b>tunable</b>

approximation (RPA), including their dependence on emitter size, gate voltage, dielectric environment, and radiative lifetime [23–25]. In contrast to these more complete numerical response calculations, the present work isolates the analytic momentum-filtering structure responsible for the  $z^{-4}$  law and for its finite- $\ell_X$  crossover. The resulting overlap formulation makes the role of the exciton form factor explicit and turns the finite-size deviation from the  $z^{-4}$  law into a probe of the localization length. We then delimit the validity of this minimal picture by benchmarking it against the full RPA and by adding the anisotropic dielectric environment, the graphene plasmon, and multilayer/graphite gates.

Our goals are threefold. First, we cast the nonradiative ET rate  $\Gamma_{\text{ET}}(z, \omega, \mu_F, \ell_X)$  in a single transparent expression—the overlap between the exciton near field and the electronic loss function of graphene—and verify that it contains the known  $z^{-4}$  law as a limit. Second, we show that the finite size of a moiré exciton, encoded in a form factor  $F_X(q)$ , leaves a clear fingerprint in the distance dependence of the quenching that encodes the localization length  $\ell_X$ . Third, we treat graphene as a gate-tunable bath, so that Pauli blocking of its electron–hole continuum allows the nonradiative channel to be electri-

cally modulated. Throughout, we deliberately work in the long-wavelength regime: because a distance  $z$  selects in-plane momenta  $q \sim 1/z$ , the essential physics is captured without a full wave-vector-resolved loss function.

## II. THEORY

### A. Golden-rule rate as a near-field/loss-function overlap

The nonradiative ET rate follows from Fermi’s golden rule,

$$\Gamma_{\text{ET}} = \frac{2\pi}{\hbar} \sum_f |\langle g; f_{\text{bath}} | H_{\text{int}} | e; 0_{\text{bath}} \rangle|^2 \delta(E_f - E_0 - \hbar\omega), \quad (1)$$

where  $|e\rangle, |g\rangle$  are the excited and ground states of the exciton and  $|0_{\text{bath}}\rangle, |f_{\text{bath}}\rangle$  are the ground and excited states of graphene. The emitter couples to the graphene electron density  $\rho_G$  through its transition Coulomb potential  $\phi_X$ ,

$$H_{\text{int}} = \int d^2r \rho_G(\mathbf{r}) \phi_X(\mathbf{r}, z) = \sum_{\mathbf{q}} \rho_G(-\mathbf{q}) \phi_X(\mathbf{q}, z). \quad (2)$$

A near-field component of in-plane momentum  $q$  decays away from the emitter as  $e^{-qz}$ , so the transition probability carries a factor  $e^{-2qz}$ . Large- $q$  components are exponentially suppressed when the emitter is far from graphene, and a given distance  $z$  probes the electronic response around  $q \sim 1/z$ .

The sum over graphene final states in Eq. (1) is the dynamic structure factor  $S(q, \omega) = \sum_f |\langle f | \rho_G(\mathbf{q}) | 0 \rangle|^2 \delta(E_f - E_0 - \hbar\omega)$ , which by the fluctuation–dissipation theorem is proportional to the

imaginary part of the graphene density response function  $\chi_G(q, \omega)$  [26], with  $S(q, \omega) \propto [1 + n_B(\omega)] [-\text{Im} \chi_G(q, \omega)]$ . At the exciton energy  $\hbar\omega \gg k_B T$  the Bose factor  $1 + n_B \simeq 1$  and is absorbed into the overall constant. It is distinct from the Pauli phase-space smearing introduced in Eq. (8) below. The rate therefore takes the compact form

$$\Gamma_{\text{ET}}(z, \omega) \propto \int \frac{d^2q}{(2\pi)^2} |\phi_X(q, z)|^2 [-\text{Im} \chi_G(q, \omega)], \quad (3)$$

i.e. the rate is the overlap between the near-field spectrum generated by the emitter and the ability of graphene to absorb energy at the same  $(q, \omega)$ . In this convention  $\phi_X$  is the *external* transition potential generated by the exciton at the graphene plane, while  $\chi_G$  is the density response of graphene to that external potential. Screening internal to graphene is therefore contained in  $\chi_G$ , not in  $\phi_X$ , which avoids double counting; the corresponding screened-response kernel is made explicit in Sec. III E.

### B. Exciton form factor and the minimal model

For concreteness we first write the near-field factor for a perpendicular point transition dipole, which produces the potential  $\phi_X(q, z) \propto e^{-qz}$ —the dipole factor  $q$  cancels the  $1/q$  of the 2D Coulomb kernel—so  $|\phi_X|^2 \propto e^{-2qz}$ . An in-plane transition dipole gives the same exponential  $e^{-2qz}$  after angular averaging and differs only by an orientation-dependent prefactor (Appendix A); the distance and localization dependence discussed below are therefore insensitive to the precise optical-dipole orientation. (Interlayer moiré excitons additionally carry a *static* out-of-plane electric dipole—responsible for their long radiative lifetime [27] and linear Stark tunability [28], and exploited in the gate dependence below—but this is distinct from the optical transition dipole considered here.)

A moiré exciton is instead spatially extended. We model it as a point internal (interband) transition dipole modulated by a center-of-mass envelope  $\psi_X(\mathbf{R})$ , so that the near-field source—the exciton transition charge density—follows the center-of-mass probability density  $|\psi_X(\mathbf{R})|^2$ . We denote by  $F_X(q)$  the *amplitude* form factor—the Fourier transform of this normalized density—so the coupling carries one power of  $F_X$  and the rate carries  $|F_X(q)|^2$ . Microscopic factors such as the relative-coordinate wave function at zero electron–hole separation, interlayer overlap, and valley/spin optical selection rules enter the overall strength  $C(\omega)$ , whereas the center-of-mass envelope controls the momentum filtering emphasized here. For a Gaussian exciton of localization length  $\ell_X$  [ $F_X(q) = e^{-q^2 \ell_X^2 / 4}$ , derived in Appendix B],

$$|F_X(q)|^2 = \exp\left(-\frac{q^2 \ell_X^2}{2}\right), \quad (4)$$

which suppresses near-field components with  $q \gtrsim 1/\ell_X$ .

The neutral-graphene interband response at small  $q$  is  $-\text{Im} \chi_G \propto q^2/\omega$  (Appendix A); with the planar measure  $d^2q = 2\pi q dq$ , Eq. (3) reduces to a single radial integral,

$$\Gamma_{\text{ET}}(z, \omega, \ell_X) = C(\omega) \int_0^{q_c} dq q^3 e^{-2qz} \exp\left(-\frac{q^2 \ell_X^2}{2}\right). \quad (5)$$

Here  $C(\omega)$  collects the transition-dipole strength, dielectric environment, and graphene-response prefactors; it is independent of  $z$  and  $\ell_X$  and therefore sets only the overall scale. The upper limit  $q_c \simeq \omega/v_F$  is the kinematic cutoff above which a Dirac electron–hole pair can no longer conserve energy and momentum. With  $\hbar v_F = 0.658$  eV nm and  $\hbar\omega = 1.5$  eV one has  $q_c \approx 2.3$  nm<sup>-1</sup> ( $1/q_c \approx 0.4$  nm), so the cutoff is irrelevant for the experimentally relevant spacings  $z \gtrsim 2$  nm. The sharp cutoff is a schematic stand-in for the kinematic edge: the exact response [Eq. (A1)] has an integrable square-root singularity at  $q = q_c$ , but the near-field factor  $e^{-2qz}$  suppresses that edge exponentially, so neither the cutoff nor the precise edge shape affects the result.

The point-dipole limit  $\ell_X \rightarrow 0$  recovers, for  $q_c \rightarrow \infty$ ,

$$\Gamma_{\text{ET}} \propto \int_0^\infty dq q^3 e^{-2qz} = \frac{3}{8z^4}, \quad (6)$$

the  $z^{-4}$  law of Refs. [1, 2]. For  $\ell_X > 0$  the Gaussian factor removes the high- $q$  part of the near field and the rate falls below the point-dipole value once  $z \lesssim \ell_X$ .

### C. Gate tunability: Pauli blocking

Doping graphene to a Fermi level  $\mu_F$  blocks interband transitions whose final state is already occupied. A vertical interband Dirac transition of energy  $\hbar\omega$  requires an empty final state, available only when  $\hbar\omega > 2|\mu_F|$ . This gate-tunable Pauli blocking of the interband absorption is well documented in graphene optical spectroscopy [29, 30]. As a first step we adopt the sharp Pauli-blocking model

$$\mathcal{L}_G(q, \omega, \mu_F) = \mathcal{L}_0(q, \omega) \Theta(\hbar\omega - 2|\mu_F|), \quad (7)$$

where  $\mathcal{L}_0 = -\text{Im} \chi_G$  is the neutral-graphene loss function. The exact interband threshold tilts with momentum,  $\hbar\omega > 2|\mu_F| - \hbar v_F q$ , but the near-field filter selects  $q \sim 1/z \ll k_F$ , for which the  $\hbar v_F q$  shift is negligible. The blocking factor is then effectively  $q$ -independent and multiplies  $\Gamma_{\text{ET}}$  as a whole, suppressing the interband contribution above  $|\mu_F| = \hbar\omega/2$ . The full momentum-resolved version is the RPA polarizability of Sec. III E. At finite temperature the interband edge is thermally smeared; the  $q \rightarrow 0$  (optical) graphene interband response gives the rigorous form [31]

$$\Theta(\hbar\omega - 2|\mu_F|) \rightarrow \frac{1}{2} \sum_{\pm} \tanh \frac{\hbar\omega \pm 2|\mu_F|}{4k_B T}, \quad (8)$$

which reduces to the step as  $T \rightarrow 0$  and broadens the threshold over  $\sim 4k_B T$  ( $\approx 0.1$  eV at room temperature). A more complete treatment would use the full Dirac-electron RPA response [26, 32], including the intraband (Drude/plasmon) channel; we develop this in Sec. III E.

#### D. From rates to PL observables

The total exciton decay rate is  $\Gamma_{\text{tot}} = \Gamma_{\text{rad}} + \Gamma_{\text{nr}}^0 + \Gamma_{\text{ET}}$ , with  $\Gamma_{\text{rad}}$  the radiative rate and  $\Gamma_{\text{nr}}^0$  the intrinsic (graphene-free) nonradiative rate. The PL lifetime is  $\tau_{\text{PL}} = 1/\Gamma_{\text{tot}}$  and the PL intensity is proportional to the quantum yield  $\Gamma_{\text{rad}}/\Gamma_{\text{tot}}$ . To avoid committing to a microscopic value of the prefactor  $C$ , we normalize to the *graphene quenching distance*  $d_0$ , defined as the point-dipole, far-field distance at which  $\Gamma_{\text{ET}} = \Gamma_0 \equiv \Gamma_{\text{rad}} + \Gamma_{\text{nr}}^0$ . This is the graphene analogue of the Förster radius and absorbs  $C$  entirely; the representative  $d_0 \sim 15$  nm used below is of the same order as the graphene energy-transfer distances reported for quantum emitters [4, 7]. We use this value only as a representative scale: all trends in Fig. 4 can be rescaled for a different, experimentally determined  $d_0$ , so the predictions are statements about scaling and device design rather than about an absolute rate. Writing  $x \equiv \Gamma_{\text{ET}}/\Gamma_0$ , both observables, measured relative to the graphene-free emitter, reduce to the same function

$$\frac{\tau_{\text{PL}}}{\tau_0} = \frac{I_{\text{PL}}}{I_0} = \frac{1}{1+x}, \quad x = \frac{\Gamma_{\text{ET}}(z, \ell_X, \mu_F)}{\Gamma_{\text{ET}}(d_0, 0, 0)}. \quad (9)$$

That the relative PL intensity and lifetime coincide when only  $\Gamma_{\text{ET}}$  varies is itself a testable prediction: graphene quenching must suppress brightness and shorten lifetime by the same factor. Equation (9) assumes the radiative rate  $\Gamma_{\text{rad}}$  is unchanged by graphene. At the nanometric spacings of interest this is the dominant nonradiative (near-field) regime, whereas modifications of  $\Gamma_{\text{rad}}$  are a far-field (radiative) correction suppressed by  $(\omega z/c)$  that we neglect here.

### III. RESULTS

All curves below use  $\hbar\omega = 1.5$  eV (a representative TMDC interlayer-exciton energy),  $\hbar v_F = 0.658$  eV nm, and, where a scale is needed, a quenching distance  $d_0 = 15$  nm and room temperature  $T = 300$  K for the interband edge [Eq. (8)].

#### A. Benchmark: recovery of the $z^{-4}$ law

Figure 2 shows the point-dipole rate  $\Gamma_0(z) = C \int_0^{q_c} dq q^3 e^{-2qz}$ . On a log-log scale it follows a slope of  $-4$  over the entire experimentally relevant range; a power-law fit for  $z > 20$  nm gives an exponent of  $-4.0000$ ,

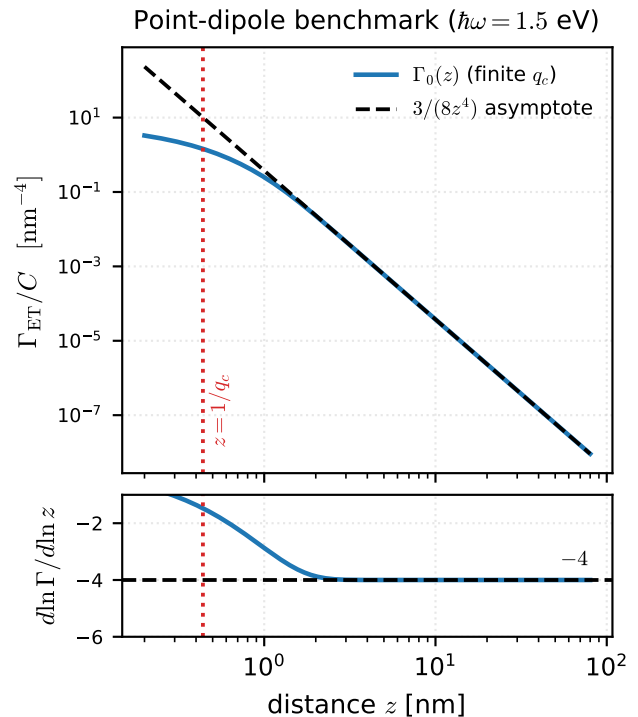


FIG. 2. Benchmark in the point-dipole limit ( $\ell_X = 0$ ). Top: ET rate (solid) and the  $3/(8z^4)$  asymptote (dashed); the vertical line marks  $z = 1/q_c$ . Bottom: local logarithmic slope, approaching  $-4$  at large  $z$ .

confirming that the numerical evaluation recovers the analytic limit Eq. (6) of Refs. [1, 2, 4]. The finite cutoff  $q_c$  bends the curve below the  $z^{-4}$  asymptote only for  $z \lesssim 1/q_c \sim 0.4$  nm, far below any realistic hBN spacer, so the cutoff plays no role in practice.

#### B. Finite-size effect: quenching as a probe of localization

Figure 3 shows the effect of the exciton form factor for  $\ell_X = 0$ –20 nm. For  $z \gg \ell_X$  the near field is dominated by  $q \sim 1/z \ll 1/\ell_X$ ,  $F_X \simeq 1$ , and all curves merge onto the point-dipole  $z^{-4}$  asymptote. For  $z \lesssim \ell_X$  the Gaussian form factor cuts the high- $q$  near field and the rate is strongly suppressed. The crossover is set by the localization length: the deviation from the  $z^{-4}$  law begins once  $z$  becomes comparable to  $\ell_X$ , with the half-suppression point—where  $\Gamma_{\text{ET}}(\ell_X)$  falls to half of the point-dipole value—appearing at  $z \approx 1.6\ell_X$  for the Gaussian model [panel (b)]. The onset of deviation from the  $z^{-4}$  law is thus sensitive to  $\ell_X$  and provides a route to extracting it. A size dependence of the energy transfer to graphene has been noted for quantum dots [23]; for moiré excitons the relevant size  $\ell_X$  is intrinsic and twist-tunable, which is what makes the deviation a spectroscopy of the localization length rather than a fixed material parameter.

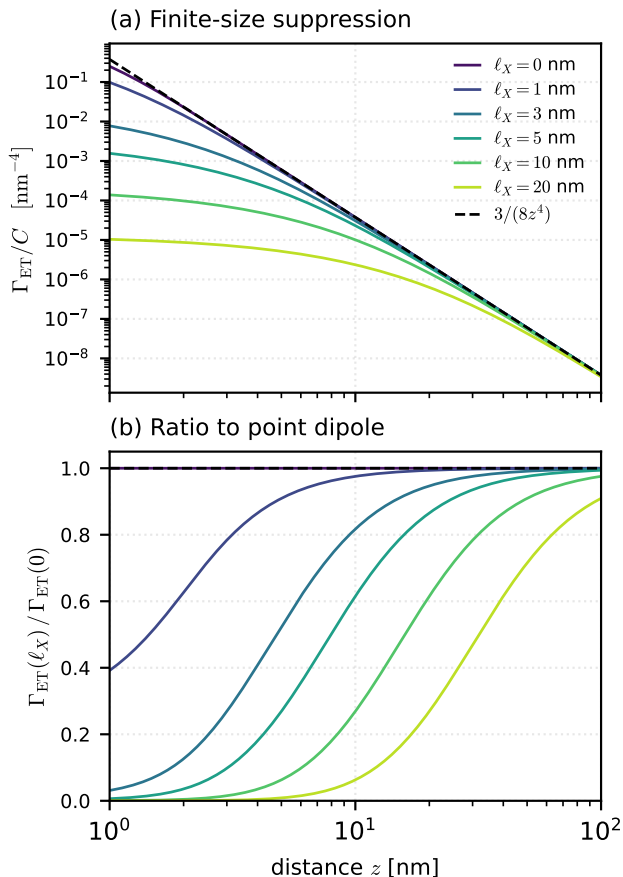


FIG. 3. Finite-size effect (common distance axis). (a)  $\Gamma_{\text{ET}}(z)$  for several localization lengths  $\ell_X$ ; the dashed line is the point-dipole asymptote. (b) Ratio to the point dipole, showing that deviations set in at  $z \sim \ell_X$ .

### C. Gate dependence: Pauli-blocked bath

Figure 4(a) shows the suppression of  $\Gamma_{\text{ET}}$  with graphene Fermi level. In the minimal model the interband channel is strongly suppressed as  $2|\mu_F|$  approaches  $\hbar\omega$ , i.e.  $|\mu_F| \rightarrow \hbar\omega/2$  (0.65, 0.75, and 0.85 eV for  $\hbar\omega = 1.3, 1.5, 1.7$  eV), thermally broadened over  $\sim 4k_B T$  at finite temperature [Eq. (8)]. Residual intraband absorption, disorder, and many-body effects make the suppression strong but not complete in practice. The  $(\hbar\omega, |\mu_F|)$  map [panel (d)] separates an active region, where graphene is a strong quencher, from a Pauli-blocked region where its interband absorption is strongly suppressed. This is the mechanism behind electrically controlled relaxation pathways [7], here applied to moiré excitons.

### D. PL observables and parameter regimes

Translating to observables through Eq. (9), Fig. 4(b,c) shows the relative PL intensity and lifetime. At  $z = 5$  nm and  $\mu_F = 0$  a point-dipole emitter is strongly quenched,  $I_{\text{PL}}/I_0 \approx 0.01$ , but a spatially extended localized exciton with  $\ell_X = 10$  nm recovers to  $\approx 0.16$  because its form factor suppresses the high- $q$  coupling. Gating graphene past  $|\mu_F| = \hbar\omega/2$  partially restores the PL even at fixed distance [panel (c)], providing an independent, electrical means of distinguishing graphene-induced quenching from disorder.

Figure 4(e,f) maps the quenching factor over the device parameter space. In the  $(z, \ell_X)$  plane [panel (e)], the contour  $I_{\text{PL}}/I_0 = 0.9$  at which quenching becomes negligible lies near  $z \approx 24$ – $26$  nm and depends only weakly on  $\ell_X$ , while strong quenching ( $< 0.5$ ) dominates below  $z \sim 10$ – $15$  nm. In the  $(z, |\mu_F|)$  plane [panel (f)], gating above  $\hbar\omega/2$  lifts the entire quenched region. These maps delineate when proximity-induced ET must be included in the interpretation of moiré-exciton PL.

### E. Beyond the minimal model: full RPA loss function

To test the minimal model we replace the heuristic factor in Eq. (5) by the genuine loss function of doped graphene, as also used for moiré-exciton quenching in Ref. [25]. The non-interacting polarizability  $\Pi(q, \omega)$  at  $T = 0$  is known in closed form [26, 32, 33]; we use their convention, in which  $\Pi(q \rightarrow 0, 0) = D_0 = gE_F/2\pi\hbar^2v_F^2 > 0$  ( $g = 4$ ) and the RPA dielectric function is  $\varepsilon(q, \omega) = 1 + v_q\Pi$  with  $v_q = 2\pi e^2/(\kappa q)$ , so the screened density response is  $\chi_{\text{RPA}} = -\Pi/\varepsilon$  and the loss function is

$$L(q, \omega, \mu_F) = -\text{Im} \chi_{\text{RPA}} = \text{Im} \left[ \frac{\Pi(q, \omega)}{\varepsilon(q, \omega)} \right], \quad (10)$$

which contains the intraband and interband single-particle continua, their Pauli-blocked phase space at finite  $\mu_F$ , and the screened plasmon. Since the emitter couples through its *bare* near-field potential  $\phi_X$  [Eq. (3)], the relevant kernel is the screened density response  $-\text{Im} \chi_{\text{RPA}} = \text{Im}[\Pi/\varepsilon]$ , not the energy-loss function  $-\text{Im}(1/\varepsilon)$ . The two are not independent: since  $1/\varepsilon = 1 + v_q\chi_{\text{RPA}}$ , one has  $-\text{Im}(1/\varepsilon) = v_q(-\text{Im} \chi_{\text{RPA}})$ , differing only by the factor  $v_q \propto 1/q$  that  $\phi_X$  already supplies. The transfer rate is then

$$\Gamma_{\text{ET}} \propto \int_0^\infty q dq e^{-2qz} |F_X(q)|^2 L(q, \omega, \mu_F), \quad (11)$$

with  $|F_X|^2$  as in Eq. (4). We verified our implementation of  $\Pi$  against the closed-form static limit [34],  $\Pi(q, 0) = D_0$  for  $q < 2k_F$ , the positivity of  $\text{Im} \Pi$  in this convention (so that  $-\text{Im} \chi_{\text{RPA}} > 0$  is the energy loss), the neutral-graphene interband form  $\text{Im} \Pi = q^2/(4\sqrt{\omega^2 - v_F^2 q^2})$ , and the existence of a  $\sqrt{q}$  plasmon.

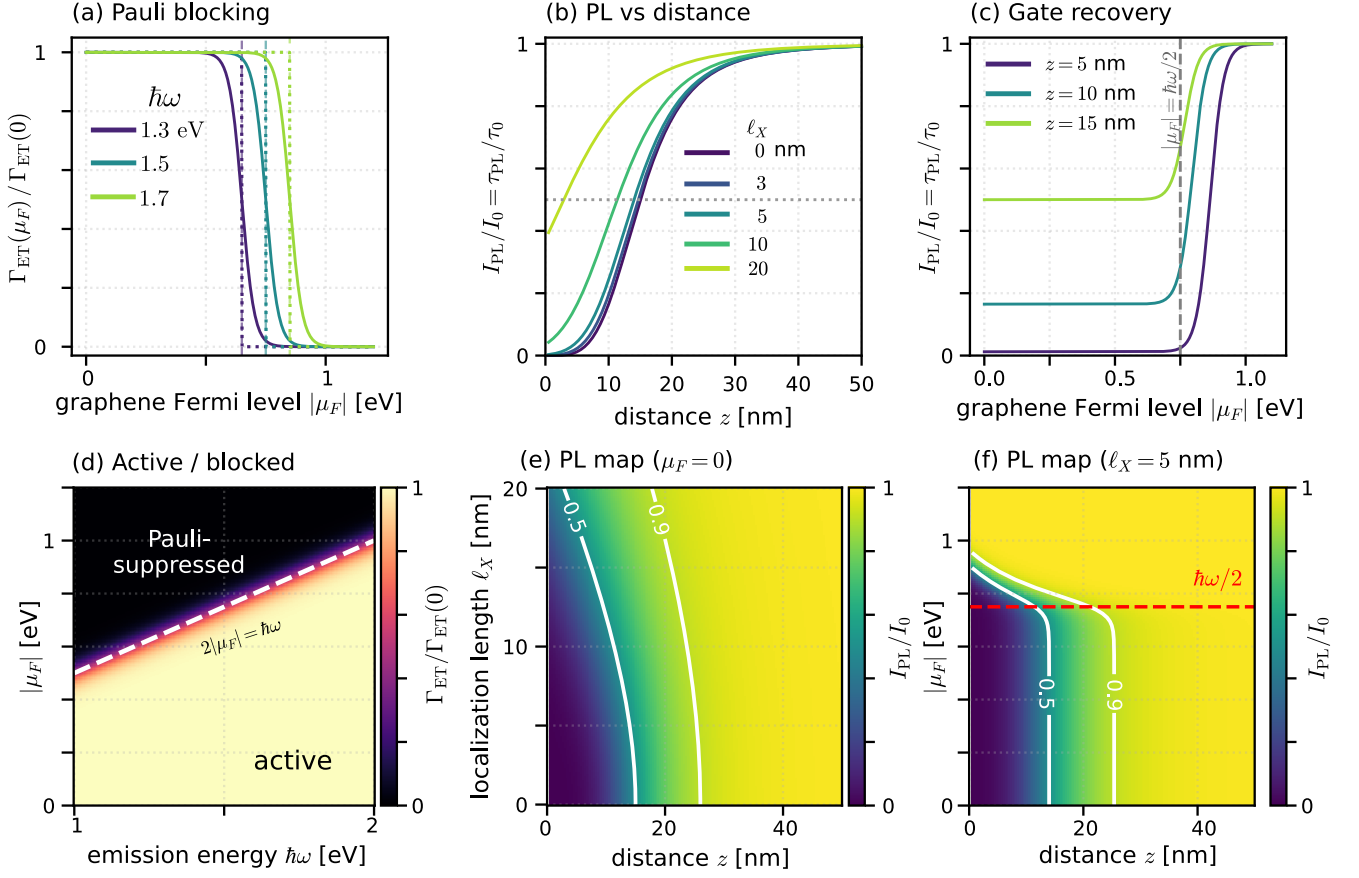


FIG. 4. Gate tunability and PL observables. Top row (curves): (a) ET suppression factor versus  $|\mu_F|$  for three emission energies (solid:  $T = 300$  K; dotted:  $T = 0$  step; vertical dashed:  $|\mu_F| = \hbar\omega/2$ ); (b) relative PL  $I_{\text{PL}}/I_0 = \tau_{\text{PL}}/\tau_0$  versus distance for several  $\ell_X$  at  $\mu_F = 0$ ; (c) the same versus Fermi level at fixed distance, showing gate-induced recovery. Bottom row (maps): (d) active versus Pauli-blocked regions in the  $(\hbar\omega, |\mu_F|)$  plane; (e) PL map in  $(z, \ell_X)$  at  $\mu_F = 0$ ; (f) PL map in  $(z, |\mu_F|)$  at  $\ell_X = 5$  nm (red dashed:  $|\mu_F| = \hbar\omega/2$ ; white contours 0.5, 0.9).

Figure 5 shows the result for hBN-encapsulated graphene ( $\kappa = 4.5$ ,  $\alpha = e^2/\kappa\hbar v_F \approx 0.49$ ; this representative value agrees to within  $\sim 12\%$  with  $\kappa_{\text{eff}} = \sqrt{\varepsilon_{\parallel}\varepsilon_{\perp}} \simeq 5.1$  from Sec. III F, and the small- $q$  result below is independent of  $\kappa$  since  $\varepsilon \rightarrow 1$  there). At the exciton emission energy  $\hbar\omega = 1.5$  eV  $\gg E_F$ , the response is interband-dominated. At small  $q$ —the only momenta that survive the  $e^{-2qz}$  near-field filter at experimentally relevant  $z$ —the screened loss function converges to the neutral-graphene interband result, because  $\text{Re}\Pi \rightarrow 0$  there and  $\varepsilon \rightarrow 1$ . Doping (Pauli blocking of part of the interband phase space) and screening only suppress  $L$  at intermediate  $q$ . Consequently the full-RPA rate follows the  $z^{-4}$  law at large  $z$  (fitted slope  $-3.998$ ) and, for the representative parameters of Fig. 5, agrees with the minimal model to within a few percent for  $z \gtrsim 3$  nm, deviating by  $\lesssim 10\%$  only at  $z \approx 2$  nm. The minimal model Eq. (5) is therefore quantitatively reliable in the regime of interest, and genuine Fermi-level control of the rate at this emission energy requires reaching the Pauli threshold  $|\mu_F| > \hbar\omega/2$ , consistent with Sec. III above.

## F. Anisotropic hBN spacer

The dielectric environment is known to influence moiré-exciton energy transfer to graphene [25]; here we make the role of the spacer anisotropy explicit. The hBN spacer is a uniaxial dielectric with in-plane permittivity  $\varepsilon_{\parallel}$  and out-of-plane  $\varepsilon_{\perp}$ . Solving the anisotropic Laplace equation  $\varepsilon_{\parallel}q^2\phi = \varepsilon_{\perp}\phi''$  for an in-plane mode  $q$  shows that the near field decays vertically as  $e^{-\gamma qz}$  with

$$\gamma = \sqrt{\varepsilon_{\parallel}/\varepsilon_{\perp}}, \quad (12)$$

so anisotropy enters the rate only through the replacement  $z \rightarrow \gamma z$  in the near-field factor (the in-plane form factor is unchanged), while the coupling is screened by  $\kappa_{\text{eff}} = \sqrt{\varepsilon_{\parallel}\varepsilon_{\perp}}$ , taken in the local-dielectric limit where  $\kappa_{\text{eff}}$  is  $q$ -independent. For bulk hBN,  $\varepsilon_{\parallel} \simeq 6.93$  and  $\varepsilon_{\perp} \simeq 3.76$  [35] give  $\gamma \simeq 1.36$  and  $\kappa_{\text{eff}} \simeq 5.1$ . As shown in Fig. 6(a,b), the  $z^{-4}$  rate is then suppressed by  $\gamma^4 \simeq 3.4$  relative to an isotropic treatment, and the graphene quenching distance shrinks by  $1/\gamma \simeq 0.74$  (a  $\sim 36\%$

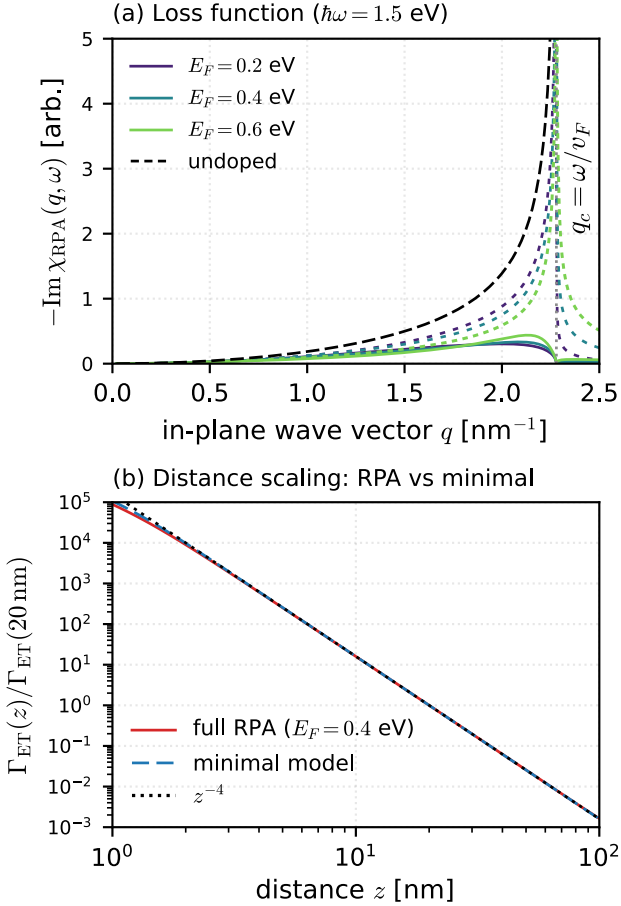


FIG. 5. Full-RPA loss function. (a)  $L(q, \omega)$  at  $\hbar\omega = 1.5$  eV for several Fermi levels (solid: screened RPA; dotted: bare bubble; dashed: neutral-graphene interband reference). (b)  $\Gamma_{\text{ET}}(z)$  from the RPA loss (red) versus the minimal model (blue), each normalized at  $z = 20$  nm; both follow  $z^{-4}$  (dotted), deviating only at small  $z$ .

overestimate of the range if anisotropy is neglected)—a correction that matters when extracting  $\ell_X$  or  $d_0$  from data.

### G. Plasmon-resonant regime and validity boundary

Besides the interband continuum, the RPA loss function (10) hosts a  $\sqrt{q}$  plasmon pole in the single-particle gap [Fig. 6(c)], the basic collective mode of graphene plasmonics [36, 37]. Energy transfer is resonantly enhanced—and departs from the  $z^{-4}$  law—when the emission energy matches the plasmon at the momenta admitted by the near-field filter  $e^{-2qz}$ , whose cutoff scale is  $q \sim 1/2z$ , i.e.  $\hbar\omega \simeq \hbar\omega_{\text{pl}}(q \sim 1/2z)$  (the rate integrand  $q^3 e^{-2qz}$  in fact peaks at  $q = 3/2z$ , which would raise the estimate by only  $\sqrt{3}$ ). These estimates ( $q \sim 1/z$ ,  $1/2z$ ,  $3/2z$ ) differ only by numerical factors of order unity and

all express the same near-field momentum scale set by the inverse spacer thickness. Graphene plasmons are, however, mid-infrared: at  $E_F = 0.4$  eV the resonant energy  $\omega_{\text{res}}(z) = \omega_{\text{pl}}(1/2z)$  ranges only  $\sim 80$ – $170$  meV for  $z = 20$ – $5$  nm [Fig. 6(d)], and even with the  $\sqrt{3}$  factor remains nearly an order of magnitude below TMDC exciton energies (1.1–1.8 eV). The plasmon channel is therefore off-resonant for moiré excitons—which lie well within the interband regime where the minimal model holds—and would dominate only for infrared emitters or much higher doping. This scale separation delimits the validity of the interband-based theory: for visible/near-infrared moiré-exciton PL, the collective mode can be neglected and Eq. (5) applies; coupling to the plasmon becomes a distinct, distance-tunable resonance only in the infrared. Throughout we use the non-retarded (electrostatic) near field and the correspondingly non-retarded  $\sqrt{q}$  plasmon dispersion. This is justified because energy transfer is dominated by in-plane momenta  $q \sim 1/2z \gg \omega/c$ , far above the light line where retardation modifies the dispersion; retardation becomes important only at much longer wavelengths, where it drives a crossover from linear to sublinear plasmon dispersion in graphene [38].

## IV. DISCUSSION

The theory above is deliberately minimal, and its assumptions delimit its scope. The Gaussian form factor (4) is the simplest model of a localized exciton. A specific moiré wave function would modify  $F_X(q)$  at large  $q$  but not the qualitative result that ET probes  $\ell_X$ . The bath and the emitter contribute in distinct distance regimes. The long-distance  $z^{-4}$  asymptote reflects the small- $q$  response of the graphene bath and is independent of the emitter’s internal structure, so it is recovered for molecules and free excitons alike. The short-distance crossover and its  $\ell_X$  dependence are where the finite-size—and hence tunable moiré—character is essential. The same formalism applies to disorder-localized monolayer excitons (with  $\ell_X$  replaced by a random  $\ell_{\text{dis}}$ ); the advantage of moiré excitons is that  $\ell_X$  is set by twist angle and moiré depth rather than by uncontrolled disorder. In practice both contributions coexist, and the resulting spatial inhomogeneity of moiré-exciton PL can be mapped and statistically disentangled by hyperspectral imaging and descriptor-correlation analyses [18, 39]. The theory should thus be read as a general exciton-to-graphene energy-transfer formalism, with moiré excitons providing the most controlled realization of a finite and tunable emitter form factor.

The same reasoning clarifies what changes if the graphene gate is replaced by multilayer graphene or graphite, as in many real devices. The  $z^{-4}$  law is specific to a single 2D sheet. A simple independent-layer estimate, in which a stack at interlayer spacing  $d \simeq 0.34$  nm contributes as  $\sum_{n \geq 0} \Gamma_{\text{ET}}^{(1)}(z + nd) \sim \int_z^\infty dz'/z'^4 \sim 1/(3d z^3)$  for  $z \gg d$ , suggests a crossover

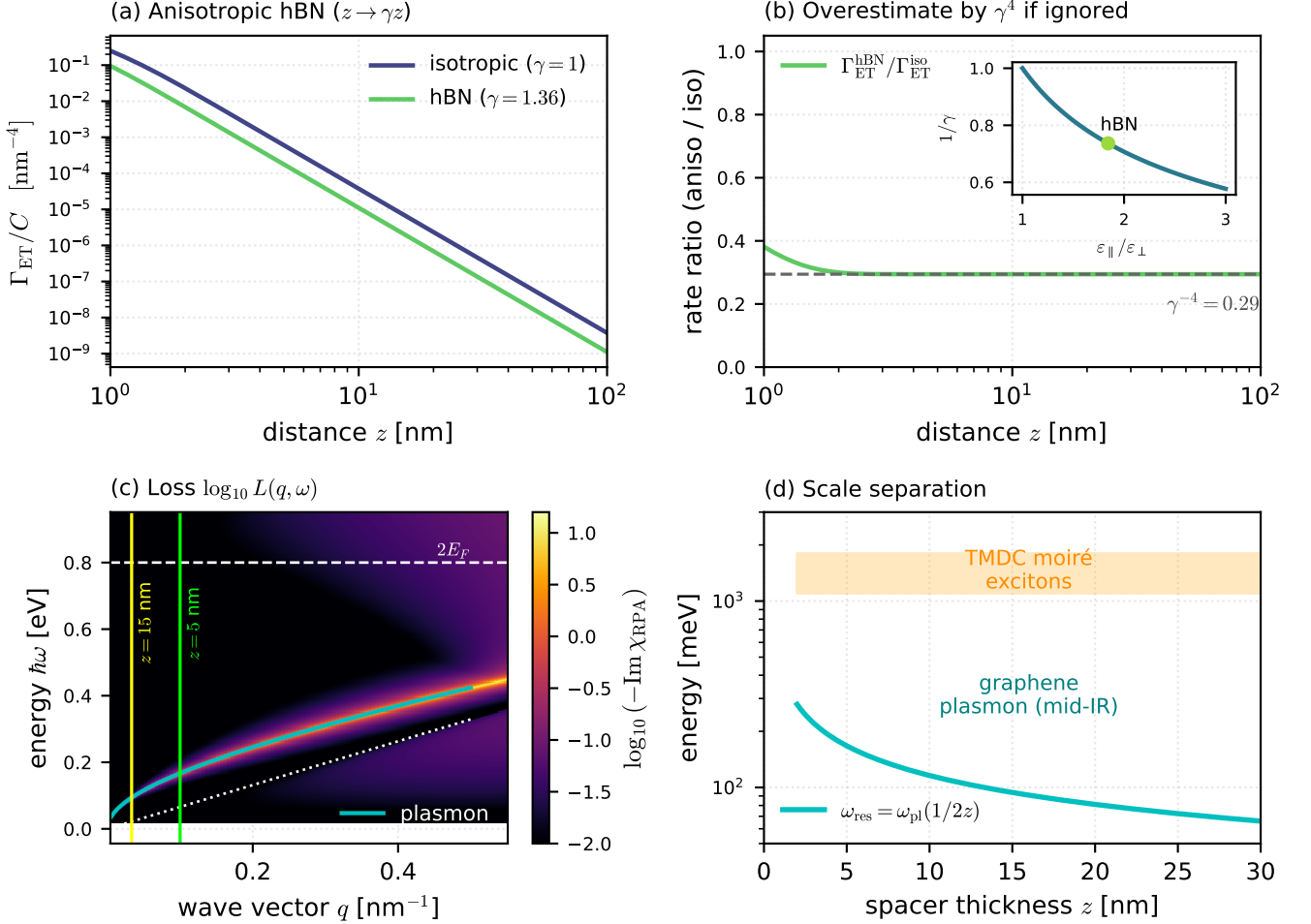


FIG. 6. Validity checks of the interband minimal model. Top row (anisotropic hBN spacer): (a) point-dipole  $\Gamma_{\text{ET}}(z)$  for an isotropic spacer ( $\gamma = 1$ ) and bulk hBN ( $\gamma = 1.36$ ; anisotropy acts as  $z \rightarrow \gamma z$ ); (b) the rate ratio plateaus at  $\gamma^{-4} \simeq 0.29$  at large  $z$ , inset the quenching-distance factor  $1/\gamma$  versus  $\varepsilon_{\parallel}/\varepsilon_{\perp}$  with bulk hBN marked. Bottom row (plasmon regime): (c) RPA loss  $\log_{10} L(q, \omega)$  at  $E_F = 0.4$  eV showing the  $\sqrt{q}$  plasmon ridge below the interband region, with near-field windows  $q \sim 1/2z$  for  $z = 5, 15$  nm; (d) the resonant energy  $\omega_{\text{pl}}(1/2z)$  versus spacer thickness lies in the mid-infrared, well separated from the TMDC moiré-exciton band.

toward  $\Gamma_{\text{ET}} \propto z^{-3}$ , consistent with the bulk surface-energy-transfer law for a molecule near an absorbing half-space [40]; few-layer stacks interpolate between the two powers. A realistic treatment would replace this layer sum by the graphite bulk and surface dielectric response (interlayer coupling and screening), but the qualitative trend is robust. Graphite is therefore expected to quench more strongly and over a longer range, by a factor of order  $z/3d$  ( $\sim 5$  at  $z = 5$  nm) within this crude independent-layer estimate, and to shift the reference power for the finite-size deviation from  $z^{-4}$  toward  $z^{-3}$ . The localization-length fingerprint, being an emitter-side effect, is unchanged, and the layer sum should be read as a scaling argument rather than a quantitative prediction for graphite. Gate tunability, by contrast, is largely lost:  $c$ -axis screening confines electrostatic doping to the top one or two layers, so Pauli blocking removes only a

fraction  $\sim d/z$  of the response while the neutral interior continues to absorb. An electrically switchable nonradiative bath is thus specific to monolayer (or few-layer) graphene, whereas a graphite gate acts as a permanently active, longer-ranged quencher.

The sharp Pauli-blocking factor (7) omits the intraband (Drude) channel and plasmonic enhancement contained in the full RPA polarizability. We showed in Sec. III E that, at the exciton emission energy  $\hbar\omega \gg E_F$ , these corrections are confined to intermediate momenta and leave the minimal model accurate for  $z \gtrsim 3$  nm. Plasmonic enhancement of the transfer is confined to the mid-infrared (Sec. III G), off-resonant for visible/near-infrared moiré excitons. Finite temperature and the anisotropic hBN dielectric environment are included above [Eqs. (8) and (12)]; both fit naturally within the overlap form (3) without altering its structure.

A further channel not treated here is direct interlayer charge transfer, which can compete with energy transfer in directly contacted graphene–TMDC stacks [41]; the present theory addresses the nonradiative *energy*-transfer pathway, which dominates once a few nanometers of hBN suppress the wave function overlap required for tunneling while leaving the long-range Coulomb coupling intact. Consistent with this picture, a recent distance-resolved study of WS<sub>2</sub>/graphene found Förster-type energy transfer to dominate at finite spacer thickness, with a Dexter (tunneling) contribution only at direct contact [42]. Energy transfer that quenches and spectrally filters the photoluminescence of an atomically thin semiconductor placed next to graphene has indeed been observed directly [43], and rapid interlayer energy transfer between dissimilar TMDC monolayers is likewise well established experimentally [44] and theoretically [45].

Two features make the predictions experimentally testable. First, because the relative PL intensity and lifetime are predicted to track each other, Eq. (9), a measured correlation between brightness and lifetime as a function of spacer thickness is an important diagnostic signature of ET rather than of varying disorder, especially when combined with gate tuning. In practice  $I_{\text{PL}}$  is also affected by excitation absorption, collection efficiency, exciton diffusion, and trap capture, so the equality  $I_{\text{PL}}/I_0 = \tau_{\text{PL}}/\tau_0$  should be read as a diagnostic limit in which only  $\Gamma_{\text{ET}}$  varies; lifetime measurements, being insensitive to these factors, provide the cleaner experimental test. Second, the gate dependence provides an *in situ* control: the same device can be driven from the active to the Pauli-blocked regime, and the recovery of PL above  $|\mu_F| = \hbar\omega/2$  isolates the graphene contribution. The required  $|\mu_F| \sim 0.6\text{--}0.8$  eV is demanding for conventional hBN-gated devices at visible exciton energies, but becomes more accessible for the lower-energy interlayer excitons ( $\hbar\omega \sim 1.1\text{--}1.4$  eV,  $|\mu_F| \sim 0.55\text{--}0.7$  eV), for infrared emitters, or for devices using strong electrostatic or ionic gating; gate control of interlayer-exciton dynamics in such devices is already established [46]. The universal distance scaling and gate control already demonstrated for point emitters [4, 7] support the underlying mechanism; the new, testable element here is the dependence on the moiré-exciton localization length. We stress, however, that a quantitative extraction of  $\ell_X$  requires an independently calibrated spacer thickness and reference quenching distance  $d_0$ , together with a lifetime-based separation of graphene-induced ET from other nonradiative channels (disorder, exciton diffusion, trap capture, and— at the smallest spacings—charge transfer). The finite-size deviation from the  $z^{-4}$  law probes  $\ell_X$  only once these contributions are controlled.

## V. CONCLUSION

We have formulated nonradiative energy transfer from moiré excitons to graphene as the overlap between the ex-

citon near-field spectrum and the long-wavelength electronic loss function of graphene, weighted by an exciton form factor. The framework reproduces the known  $z^{-4}$  law in the point-dipole limit, predicts a localization-length-dependent suppression that turns PL quenching into a spectroscopy of moiré-exciton extent, and— through Pauli blocking—makes the nonradiative channel electrically tunable. The cleanest experimental test is a spacer-thickness-dependent lifetime measurement, in which the departure from the  $z^{-4}$  law provides a route to extracting the moiré-exciton localization length. Gate tuning of the bath is most favorable for low-energy interlayer excitons and, more generally, for infrared emitters, where the Pauli threshold  $|\mu_F| \sim \hbar\omega/2$  and the graphene plasmon are most accessible. In van der Waals exciton devices, a graphene gate should therefore be regarded not as a passive electrostatic element but as a tunable 2D nonradiative reservoir whose long-wavelength response can be probed through exciton photoluminescence quenching.

## ACKNOWLEDGMENTS

This work was supported by JSPS KAKENHI (Grants No. JP25K01609 and No. JP22H05473).

### Appendix A: Neutral-graphene response and the $q^3$ kernel

The minimal kernel of Eq. (5) follows from the standard small- $q$ , Dirac-cone density response of neutral graphene. At  $T = 0$  and for  $\omega > v_F q$ , the imaginary part of the noninteracting polarizability is

$$-\text{Im} \chi_0(q, \omega) = \frac{g}{16} \frac{q^2}{\sqrt{\omega^2 - v_F^2 q^2}} \Theta(\omega - v_F q), \quad (\text{A1})$$

with degeneracy  $g = 4$  (we set  $\hbar = 1$  in this Appendix). The same Dirac-cone polarization, evaluated statically, gives the  $q$ -linear interband result  $\Pi^0(q) = gq/(16v_F)$  [34], sharing the  $g/16$  prefactor. For  $\omega \gg v_F q$ —the regime selected by the near-field filter at experimentally relevant  $z$ —this reduces to  $-\text{Im} \chi_0 \simeq (g/16) q^2/\omega \propto q^2/\omega$ , the form used in the main text. This long-wavelength interband response is the same physics as the frequency-independent universal optical conductance  $\sigma_0 = \pi e^2/2h$  of graphene [47], here resolved at finite  $q$ .

A transition dipole at height  $z$  couples to graphene through its bare Coulomb potential. For a dipole perpendicular to the plane, the in-plane Fourier component of the potential is  $\phi_X(q, z) \propto e^{-qz}$  (the dipole derivative  $\partial_z$  brings a factor  $q$  that cancels the  $1/q$  of the 2D Coulomb kernel  $2\pi/q$ ), so  $|\phi_X|^2 \propto e^{-2qz}$ . An in-plane dipole gives  $|\phi_X|^2 \propto \cos^2\theta e^{-2qz}$ , whose azimuthal average is  $\frac{1}{2}e^{-2qz}$ ; the orientation enters only through this

constant, absorbed into  $C(\omega)$ . Inserting both factors into the overlap form Eq. (3) with the planar measure  $d^2q = 2\pi q dq$  gives

$$\Gamma_{\text{ET}} \propto \int q dq \underbrace{e^{-2qz}}_{|\phi_X|^2} \underbrace{\frac{q^2}{\omega}}_{-\text{Im } \chi_0} = \frac{1}{\omega} \int dq q^3 e^{-2qz}, \quad (\text{A2})$$

i.e. Eq. (5) with  $C(\omega) \propto 1/\omega$ , and  $\int_0^\infty q^3 e^{-2qz} dq = 3/(8z^4)$  reproduces the Swathi–Sebastian  $z^{-4}$  law [1, 2]. The chirality factor of the Dirac matrix elements is contained in Eq. (A1) and likewise affects only the prefactor, not the  $z$ -dependence.

## Appendix B: Gaussian exciton form factor

Within the point-dipole-times-envelope model of the main text (a point internal transition dipole modulated

by a center-of-mass envelope), the near-field source profile is the center-of-mass probability density. For a 2D Gaussian envelope  $\psi_X(\mathbf{R}) \propto e^{-R^2/2\ell_X^2}$ , this normalized density is  $n_X(\mathbf{R}) = |\psi_X(\mathbf{R})|^2 \propto e^{-R^2/\ell_X^2}$ . Its Fourier transform is the amplitude form factor

$$F_X(q) = \frac{\int d^2R n_X(\mathbf{R}) e^{-iq \cdot \mathbf{R}}}{\int d^2R n_X(\mathbf{R})} = \exp\left(-\frac{q^2 \ell_X^2}{4}\right), \quad (\text{B1})$$

so the rate carries  $|F_X(q)|^2 = e^{-q^2 \ell_X^2/2}$ , Eq. (4). The point-dipole limit is  $\ell_X \rightarrow 0$ ,  $F_X \rightarrow 1$ . A different envelope changes  $F_X(q)$  only at  $q \gtrsim 1/\ell_X$  and does not alter the conclusion that energy transfer probes the localization length  $\ell_X$ .

- 
- [1] R. S. Swathi and K. L. Sebastian, *J. Chem. Phys.* **129**, 054703 (2008).
- [2] R. S. Swathi and K. L. Sebastian, *J. Chem. Phys.* **130**, 086101 (2009).
- [3] T. Förster, *Ann. Phys. (Leipzig)* **437**, 55 (1948).
- [4] L. Gaudreau, K. J. Tielrooij, G. E. D. K. Prawiroatmodjo, J. Osmond, F. J. García de Abajo, and F. H. L. Koppens, *Nano Lett.* **13**, 2030 (2013).
- [5] Z. Chen, S. Berciaud, C. Nuckolls, T. F. Heinz, and L. E. Brus, *ACS Nano* **4**, 2964 (2010).
- [6] F. Federspiel, G. Froehlicher, M. Nasilowski, S. Pedetti, A. Mahmood, B. Doudin, S. Park, J.-O. Lee, D. Halley, B. Dubertret, P. Gilliot, and S. Berciaud, *Nano Lett.* **15**, 1252 (2015).
- [7] K. J. Tielrooij, L. Orona, A. Ferrier, M. Badioli, G. Navickaite, S. Coop, S. Nanot, B. Kalinic, T. Cesca, L. Gaudreau, Q. Ma, A. Centeno, A. Pesquera, A. Zurutuza, H. de Riedmatten, P. Goldner, F. J. García de Abajo, P. Jarillo-Herrero, and F. H. L. Koppens, *Nat. Phys.* **11**, 281 (2015).
- [8] J. Lee, W. Bao, L. Ju, P. J. Schuck, F. Wang, and A. Weber-Bargioni, *Nano Lett.* **14**, 7115 (2014).
- [9] G. Gómez-Santos and T. Stauber, *Phys. Rev. B* **84**, 165438 (2011).
- [10] K. A. Velizhanin and A. Efimov, *Phys. Rev. B* **84**, 085401 (2011).
- [11] G. Wang, A. Chernikov, M. M. Glazov, T. F. Heinz, X. Marie, T. Amand, and B. Urbaszek, *Rev. Mod. Phys.* **90**, 021001 (2018).
- [12] A. Chernikov, T. C. Berkelbach, H. M. Hill, A. Rigosi, Y. Li, B. Aslan, D. R. Reichman, M. S. Hybertsen, and T. F. Heinz, *Phys. Rev. Lett.* **113**, 076802 (2014).
- [13] K. L. Seyler, P. Rivera, H. Yu, N. P. Wilson, E. L. Ray, D. G. Mandrus, J. Yan, W. Yao, and X. Xu, *Nature* **567**, 66 (2019).
- [14] K. Tran, G. Moody, F. Wu, X. Lu, J. Choi, K. Kim, A. Rai, D. A. Sanchez, J. Quan, A. Singh, J. Embley, A. Zepeda, M. Campbell, T. Autry, T. Taniguchi, K. Watanabe, N. Lu, S. K. Banerjee, K. L. Silverman, S. Kim, E. Tutuc, L. Yang, A. H. MacDonald, and X. Li, *Nature* **567**, 71 (2019).
- [15] C. Jin, E. C. Regan, A. Yan, M. I. B. Utama, D. Wang, S. Zhao, Y. Qin, S. Yang, Z. Zheng, S. Shi, K. Watanabe, T. Taniguchi, S. Tongay, A. Zettl, and F. Wang, *Nature* **567**, 76 (2019).
- [16] K. Shinokita, K. Watanabe, T. Taniguchi, and K. Matsuda, *ACS Nano* **16**, 16862 (2022).
- [17] H. Kim, K. Aino, K. Shinokita, W. Zhang, K. Watanabe, T. Taniguchi, and K. Matsuda, *Adv. Opt. Mater.* **11**, 2300146 (2023).
- [18] N. F. Ahmad, Y. Urano, K. Watanabe, T. Taniguchi, D. Kozawa, and R. Kitaura, *Appl. Phys. Lett.* **128**, 231901 (2026).
- [19] H. Yu, G.-B. Liu, J. Tang, X. Xu, and W. Yao, *Sci. Adv.* **3**, e1701696 (2017).
- [20] F. Wu, T. Lovorn, and A. H. MacDonald, *Phys. Rev. B* **97**, 035306 (2018).
- [21] K. F. Mak and J. Shan, *Nat. Nanotechnol.* **17**, 686 (2022).
- [22] H. Baek, M. Brotons-Gisbert, Z. X. Koong, A. Campbell, M. Rambach, K. Watanabe, T. Taniguchi, and B. D. Gerardot, *Sci. Adv.* **6**, eaba8526 (2020).
- [23] I. Fezai and S. Jaziri, *Superlattices Microstruct.* **109**, 71 (2017).
- [24] R. Eddhib, S. Ayari, A. Hichri, and S. Jaziri, *Phys. Rev. B* **104**, 115426 (2021).
- [25] A. Hichri, T. Amand, and S. Jaziri, *Phys. Rev. Mater.* **5**, 114002 (2021).
- [26] E. H. Hwang and S. Das Sarma, *Phys. Rev. B* **75**, 205418 (2007).
- [27] P. Rivera, J. R. Schaibley, A. M. Jones, J. S. Ross, S. Wu, G. Aivazian, P. Klement, K. Seyler, G. Clark, N. J. Ghimire, J. Yan, D. G. Mandrus, W. Yao, and X. Xu, *Nat. Commun.* **6**, 6242 (2015).
- [28] A. Ciarrocchi, D. Unuchek, A. Avsar, K. Watanabe, T. Taniguchi, and A. Kis, *Nat. Photonics* **13**, 131 (2019).

- [29] F. Wang, Y. Zhang, C. Tian, C. Girit, A. Zettl, M. Crommie, and Y. R. Shen, *Science* **320**, 206 (2008).
- [30] Z. Q. Li, E. A. Henriksen, Z. Jiang, Z. Hao, M. C. Martin, P. Kim, H. L. Stormer, and D. N. Basov, *Nat. Phys.* **4**, 532 (2008).
- [31] L. A. Falkovsky and A. A. Varlamov, *Eur. Phys. J. B* **56**, 281 (2007).
- [32] B. Wunsch, T. Stauber, F. Sols, and F. Guinea, *New J. Phys.* **8**, 318 (2006).
- [33] S. Das Sarma, S. Adam, E. H. Hwang, and E. Rossi, *Rev. Mod. Phys.* **83**, 407 (2011).
- [34] T. Ando, *J. Phys. Soc. Jpn.* **75**, 074716 (2006).
- [35] A. Laturia, M. L. Van de Put, and W. G. Vandenberghe, *npj 2D Mater. Appl.* **2**, 6 (2018).
- [36] A. N. Grigorenko, M. Polini, and K. S. Novoselov, *Nat. Photonics* **6**, 749 (2012).
- [37] F. J. García de Abajo, *ACS Photonics* **1**, 135 (2014).
- [38] H.-Y. Deng and K. Wakabayashi, *Phys. Rev. B* **92**, 045434 (2015).
- [39] K. Wakabayashi, arXiv:2606.06780 (2026).
- [40] R. R. Chance, A. Prock, and R. Silbey, *Adv. Chem. Phys.* **37**, 1 (1978).
- [41] G. Froehlicher, E. Lorchat, and S. Berciaud, *Phys. Rev. X* **8**, 011007 (2018).
- [42] D. Tebbe, M. Schütte, K. Watanabe, T. Taniguchi, C. Stampfer, B. Beschoten, and L. Waldecker, *Phys. Rev. Lett.* **132**, 196902 (2024).
- [43] E. Lorchat, L. E. Parra López, C. Robert, D. Lagarde, G. Froehlicher, T. Taniguchi, K. Watanabe, X. Marie, and S. Berciaud, *Nat. Nanotechnol.* **15**, 283 (2020).
- [44] D. Kozawa, A. Carvalho, I. Verzhbitskiy, F. Giustiniano, Y. Miyauchi, S. Mouri, A. H. Castro Neto, K. Matsuda, and G. Eda, *Nano Lett.* **16**, 4087 (2016).
- [45] C. Manolatu, H. Wang, W. Chan, S. Tiwari, and F. Rana, *Phys. Rev. B* **93**, 155422 (2016).
- [46] L. A. Jauregui, A. Y. Joe, K. Pistunova, D. S. Wild, A. A. High, Y. Zhou, G. Scuri, K. De Greve, A. Sushko, C.-H. Yu, T. Taniguchi, K. Watanabe, D. J. Needleman, M. D. Lukin, H. Park, and P. Kim, *Science* **366**, 870 (2019).
- [47] R. R. Nair, P. Blake, A. N. Grigorenko, K. S. Novoselov, T. J. Booth, T. Stauber, N. M. R. Peres, and A. K. Geim, *Science* **320**, 1308 (2008).